The Company of Biologists

RESEARCH ARTICLE

Compromise between mechanical and chemical protection mechanisms in the *Mytilus edulis* shell

Chao Wan*,‡, Yun Ma and Stanislav N. Gorb‡

ABSTRACT

The shell of *Mytilus edulis* is a multilayered system for protecting this bivalve. In contrast to well-developed research on the nacre materials, the protective function of the complete *M. edulis* shell has not been widely studied. In particular, the question of why nacre is situated on the inner side of the shell rather than on the outer side remains unclear. Herein, the acid resistance of different shell layers was compared using etching tests and the mechanical protection performance of the shell was tested using three-point bending. Two bending loads, including static and dynamic, were applied on the shell samples from outside in (i.e. out–in bending) and from inside out (i.e. in–out bending), respectively. Our etching results show that the external prismatic calcite endows *M. edulis* with stronger acid resistance than if nacre was on the outside. In contrast, the static out–in and in–out bending tests reveal that a better mechanical protection of the shell against slow mechanical attacks is achieved if the nacre is on the outside. However, the shell has the same mechanical properties against dynamic mechanical attacks regardless of nacre location. Briefly, the nacre should be on the outside of the shell for better mechanical protection while the outside location of the prismatic layer offers a stronger resistance against etching. The inside natural location of nacre is a compromise between mechanical and chemical protection mechanisms against a complex survival environment. This strongly contributes to our understanding of biological design principles and further development of shell-inspired protective materials.

KEY WORDS: Mussel shell, Nacre, Prismatic calcite, Mechanical properties, Acid resistance

INTRODUCTION

The shell is the essential armor for mussels to protect their soft bodies against predators and other environmental impacts, and consists of 95–99% calcium carbonate and less than 5% organic matrix (Zhang and Zhang, 2006; Barthelat et al., 2007; Sun and Bhushan, 2012). The blue mussel (*Mytilus edulis*) is a common bivalve mollusk that lives in intertidal zones by attaching to rough rocks and other hard substrates. The shell of *M. edulis* is composed of three layers, from outside to inside: periostracum (composed of rather stiff cross-linked proteins), prismatic layer (mainly composed of columnar calcite grains) and nacreous layer (mainly composed of

aragonite platelets), respectively (Arivalagan et al., 2016). Nacre, the material of the inner layer, has been an intense research topic for scientists and engineers for decades because of its superior strength and tolerance of flaws (Jackson et al., 1988; Menig et al., 2000). The strengthening and toughening mechanisms of nacre are also well understood (Wang et al., 2001; Gao et al., 2003; Barthelat and Espinosa, 2007; Meyers et al., 2008; Song et al., 2008; Shao et al., 2012). Based on this knowledge, materials scientists have synthesized biomimetic nacre-like material (Podsiadlo et al., 2007; Bonderer et al., 2008; Mao et al., 2016).

However, nacre is only one part of the complex three-layered mussel shell system (Fig. 1). In order to understand the defense function of the shell system as a whole, the effects on a larger scale should be considered and these have received less attention in comparison to the nano-scale research on the nacre (Ortiz and Boyce, 2008). Knowing all the mechanical qualities of the nacre, one may ask the question why nacre is deposited as an inner layer of the mussel shell and not as the external one? Preventing crack initiation/propagation might be more important at the side where the external mechanical threat is more probable.

In nature, three different strategies are frequently utilized by common predators to attack the *M. edulis* shell: (1) chemical attack of acid secretions from dog whelk gastropods; (2) mechanical attack from decapod crabs using slow crushing; and (3) mechanical attacks from gulls and other sea birds using fast strike (Day, 1969; Fänge and Lidman, 1976; Gabriel, 1981; Moody and Steneck, 1993). We hypothesized that the combination of outside prismatic calcite and inside nacre is a compromise between mechanical and chemical protection for the mussel to achieve sufficient resistance against complex survival threats. Hence, three types of experiments – acidic etching, and static and dynamic bending tests – were implemented on the shells of *M. edulis* in this study. In order to investigate the anti-acid properties of the different shell layers, the acid etching tests were carried out on the periostracum, prismatic and nacreous layers of the shell. The static and dynamic bending tests were performed on the mussel shell from outside in and inside out and further analyzed using inverse finite element (FE) optimization to obtain the mechanical properties of the shell under out–in and in–out bending. Comparison of the acid and mechanical resistance between the out–in and in–out attacks could provide us with potential reasons why nacre is deposited on the inside rather than the outside of the shell.

MATERIALS AND METHODS
Sample preparation

Fresh bivalve mussels, *M. edulis* Linnaeus 1758, bred in the Kiel fjord on an aquatic farm (Föhrer Muscheln GmbH, Niebüll, Germany) were purchased at a local supermarket (Kiel, Germany) in fresh condition. Sixty mussels of similar size were selected to minimize variation in testing results due to different mussel history or age. All the mussels were double-wrapped by gauze wetted in sea water, sealed in airtight plastic bags and stored at −20°C until tested.

Functional Morphology and Biomechanics, Zoological Institute, Kiel University, 24118 Kiel, Germany.
*Present address: Department of Mechanics, School of Aerospace Engineering, Beijing Institute of Technology, Beijing 100081, China.

‡Authors for correspondence (chaowan@bit.edu.cn; sgorb@zoologie.uni-kiel.de)

C.W., 0000-0003-2337-9968; S.N.G., 0000-0001-9712-7953
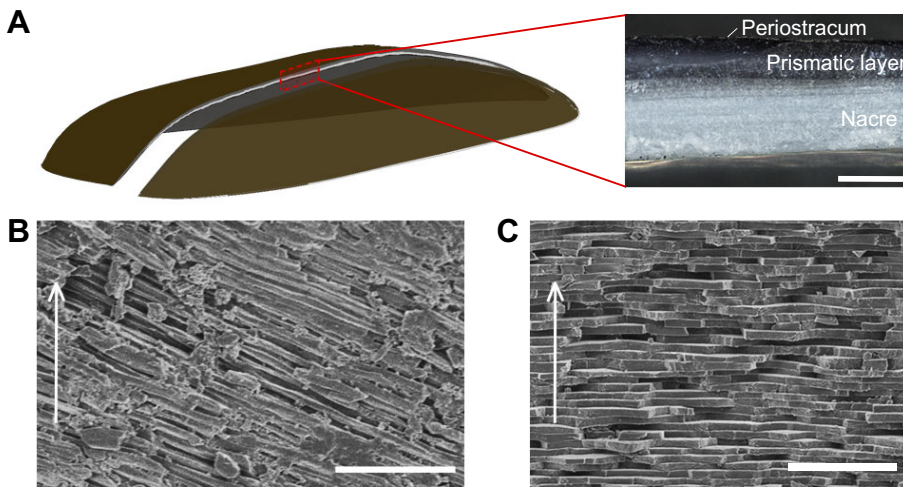
Fig. 1. Multiscale structures in *Mytilus edulis* shells. (A) Multilayered structure of the cross-section of the bivalve shell observed under an optical microscope. Three layers are visible from outside to inside: the periostracum, the prismatic layer and the nacre. (B) Scanning electron microscope (SEM) images of oblique-arranged columnar calcite grains situated in the prismatic layer. (C) SEM image of the brick-and-mortar-like structure of the nacre. White arrows in B and C indicate the normal direction of the shell from inside to outside. Scale bars: A, 600 μm; B and C, 10 μm.

Before sample cutting, the mussels were thawed at room temperature. From each mussel, only one sample of full thickness was harvested in the middle of one of its two shells (Figs 2A and 3A). A hand hacksaw was firstly used to carefully cut a larger sample from the mussel shell and then the sectional surface of the sample was finely ground using an electric hand mill (Micromot 60/E, Proxxon GmbH, Föhren, Germany) to the following final size: 24 square samples approximately 10 mm×10 mm were cut for the etching test, 24 beam samples were extracted with a minimal length of 35 mm and approximate width of 2.6 mm for the static bending test, and 12 beam samples were prepared of similar size for the dynamic bending test. Finally, the prepared sample was checked under a stereomicroscope to confirm that neither visible damage nor a jagged surface existed in the samples. The beam samples were wrapped using degreasing cotton wetted by sea water and kept in plastic centrifuge tubes to keep them moist.

Etching test

The inner surfaces of all 24 square shell samples were first polished by sandpaper (grade: P3000) to remove possible residual mantle tissues. Then, the square samples were divided into four groups (A–D, n=6 samples per group). The periostracum of the samples in group A was kept intact while that in groups B–D was removed

using a hand mill and sandpaper. Groups A–C were used for analyzing mass loss, while group D was used for analyzing the change of surface wettability after etching.

Before the etching test, the samples in groups A–C were dried in an oven at 65°C for 2 h, and weighed 3 times by a micro-balance (AG204, Mettler Toledo GmbH, Giessen, Germany). Then, pipette tips (2.6 mm diameter at the top end) filled with degreasing cotton were injected with 0.2 ml of 0.1 mol l^{-1} hydrochloric acid solution (pH 0.99) and placed on the periostracum, prismatic and nacreous surfaces of the samples in groups A, B and C, respectively (Fig. 2B). The degreasing cotton absorbed the acid solution, preventing it from spreading on the surface of the shell and producing the same etching conditions for each sample. The total etching duration was 1 h and the acid solution in the pipette tips was replaced after 0.5 h to maintain the solution concentration. The concentration of the acid solution was chosen in order to simulate the real pH of the acid salivary secretions from predators (Day, 1969; Fänge and Lidman, 1976; Morton, 2015). After the etching, all the samples were washed 3 times with distilled water, dried in an oven at 65°C for 2 h, and weighed 3 times using the micro-balance. The mass loss of each sample was calculated based on the measurements before and after etching. All the samples were manually snapped at their etching site and sputter-coated with gold–palladium (10 nm thickness) using a
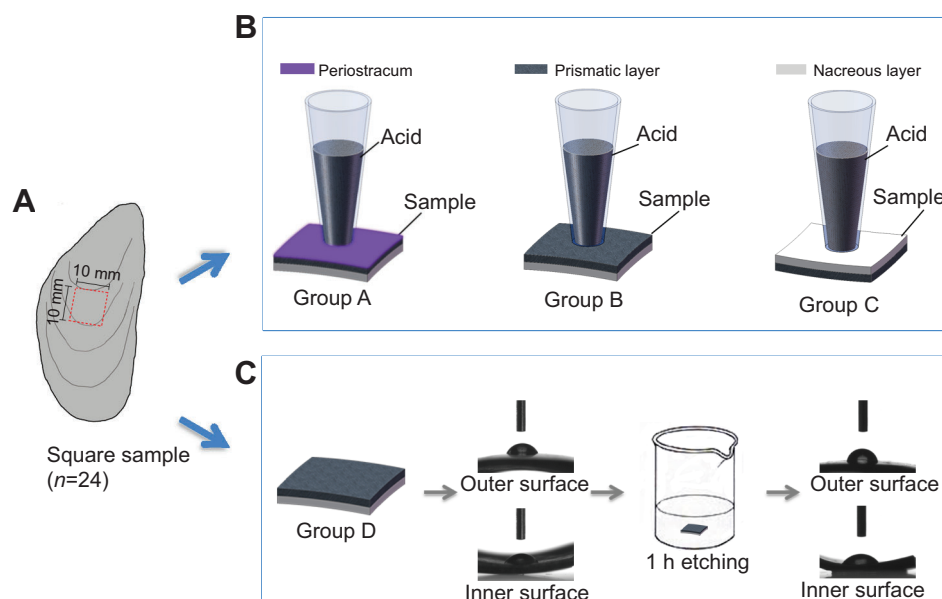
Fig. 2. Protocol for etching tests on the *M. edulis* shell. (A) Twenty-four square shell samples (approximately 10 mm×10 mm) were cut from the middle of 24 individual mussel shells (marked by a red dashed line). (B) Three groups (n=6 for each group) were designed for comparison of the mass loss caused by etching on the periostracum (group A), prismatic (group B) and nacreous (group C) layers of the shell. (C) The contact angle and area of the distilled water droplet on the outer (i.e. prismatic layer) and inner (nacreous layer) surfaces of group D (n=6) were measured before and after 1 h of etching with 0.1 mol l^{-1} hydrochloric acid solution.
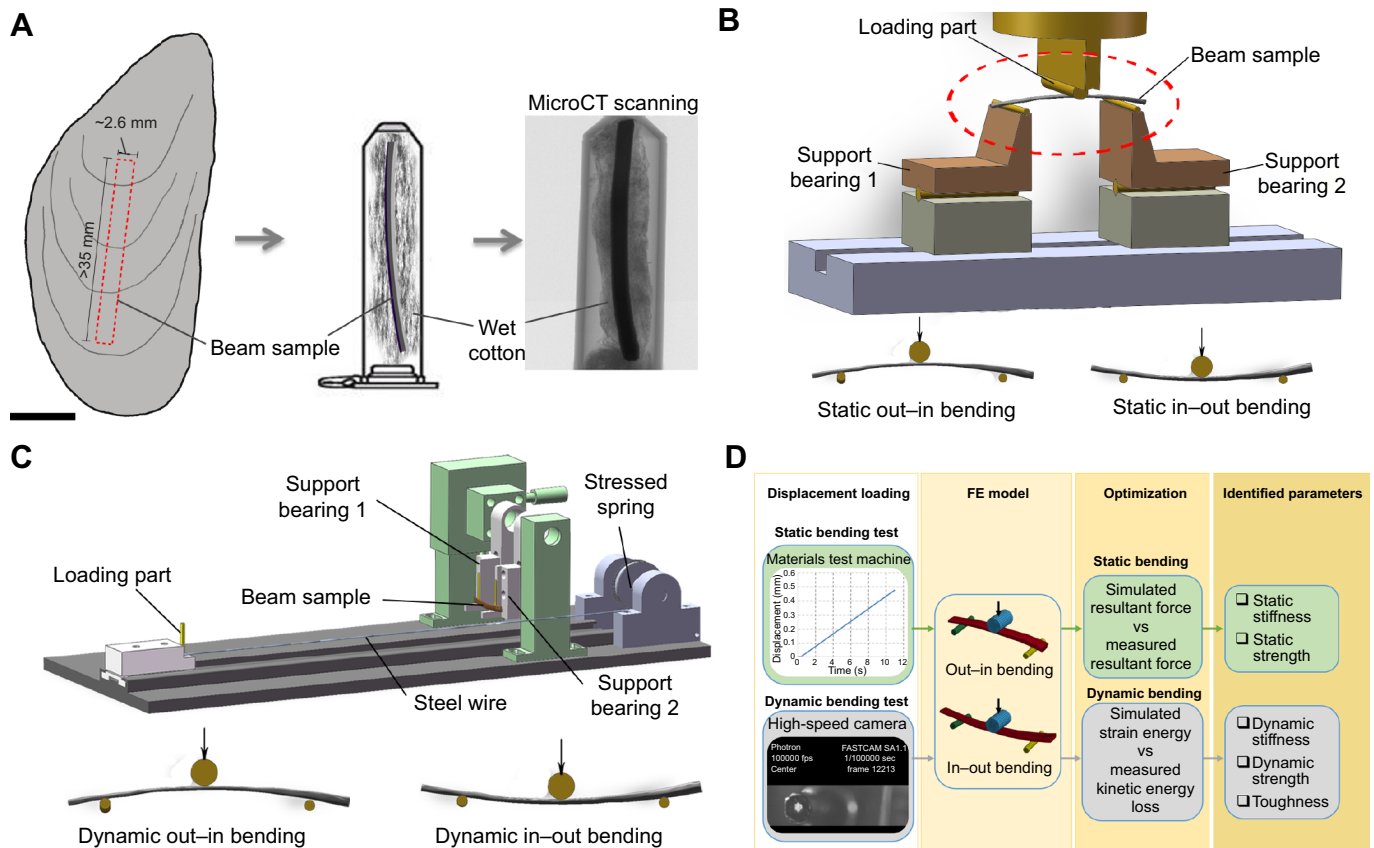
Fig. 3. Protocol for determining mechanical resistance of the *M. edulis* shell. (A) Beam samples (*n*=36) cut from the middle of mussel shells (site marked by the red dashed line) were wrapped in wet degreasing cotton inside plastic centrifuge tubes, and scanned using micro-computed tomography (microCT) prior to bending tests. (B) Static three-point bending tests were implemented on *n*=12 beam shell samples by bending from outside in (i.e. static out–in bending) as well as on *n*=12 beam shell samples by bending from inside out (i.e. static in–out bending). (C) Dynamic three-point bending tests were performed on *n*=6 beam shell samples loaded from outside in (i.e. dynamic out–in bending) and *n*=6 samples loaded from inside out (i.e. dynamic in–out bending). The loading part was actuated by releasing the stressed spring in the custom-designed build-up impact bending tester. (D) The mechanical properties of shell samples under the out–in and in–out three-point bending tests were determined by an inverse finite element (FE) optimization, including static stiffness and strength, dynamic stiffness and strength, and toughness. Experimental displacements from the materials testing machine and high-speed camera were applied in the FE models to simulate the static and dynamic bending tests, respectively. The objective function of the optimization was a resultant force curve for the static bending test and the total transfer from kinetic energy to strain energy for the dynamic bending test. Scale bar in A: 10 mm.

high-vacuum sputtercoater (Leica EM SCD500, Leica Microscopy GmbH, Wetzlar, Germany). The microstructures on the etching surface and the snapped cross-section were visualized with a scanning electronic microscope (SEM) at an accelerating voltage of 3 kV (S-4800, Hitachi High-Tech Corp., Tokyo, Japan).

The samples in group D were used for measuring the wettability of the surface (Fig. 2C). The shell surface was considered as a curve based on the lateral images. Because the droplet spread on the shell surface evenly, its contact area with the shell surface was assumed to be a spherical cap and was calculated from the images. Using a contact angle system (OCA20, DataPhysics Instruments GmbH, Filderstadt, Germany), one droplet of 1 µl distilled water ($0.5\ \mu l\ s^{-1}$) was placed in the middle of the outer (i.e. prismatic) and inner (i.e. nacreous) surfaces before and after the samples were etched by $0.1\ mol\ l^{-1}$ hydrochloric acid solution for 1 h. The contact angle of the droplet was determined based on three measurements and compared to identify whether etching affected the contact angle on the prismatic and nacreous layers.

Static and dynamic three-point bending tests

Before the bending tests, all 36 beam shell samples were scanned by micro-computed tomography (microCT; Skyscan 1172, Bruker

microCT Corp., Kontich, Belgium) (Fig. 3A). The scanning settings were 60 kV source voltage, 167 µA source current, 40 ms exposure time and 20 µm×20 µm×20 µm voxel resolution. The samples were wrapped in wet cotton inside plastic centrifuge tubes during scanning and then taken out for the bending tests. During the static and dynamic bending tests, drops of sea water were manually placed on the shell samples to avoid desiccation.

The static three-point bending tests were performed using a materials testing machine (zwickiLine Z0.5, Zwick GmbH & Co. KG, Ulm, Germany) with a fully articulated fixture apparatus (Fig. 3B). The span of the two supporting bearings was adjusted for each sample to obtain an acceptable span/thickness ratio (i.e. 15 or more) for a precise estimation of material properties (Jackson et al., 1988). Twelve beam samples were loaded at the middle of their outer surface for out–in bending and 12 samples were loaded at the middle site of their inner surface for in–out bending. A 0.1 N force was applied first and subsequent loads were applied at a strain rate of $0.05\ min^{-1}$ until sample fracture. The displacement–force curve for each sample was recorded by the materials testing machine.

The dynamic three-point bending tests were performed using a custom-designed impact bending tester with a loading part (34 mg) that was actuated by a strained spiral spring, translated on a low-

friction guideway (Igus GmbH, Köln, Germany), which impacted the samples at approximately 5.0 m s⁻¹ (Fig. 3C). Six beam samples were loaded at the middle of their outer surface and six samples were loaded at the middle of their inner surface, corresponding to dynamic out–in and in–out bending, respectively. The displacement of the loading part was recorded by a high-speed camera (PhotronFastcam SA1.1, VKT GmbH, Pfullingen, Germany) under a stereomicroscope (Leica MZ12.5). The frame rate was 100,000 frames s⁻¹ and the resolution of the images was 51 μm per pixel. The velocity of the loading part was calculated based on the image stacks using Image-Pro Plus software (Media Cybernetics Inc., Rockville, MD, USA) and used to obtain the loss of kinetic energy before loading and before sample fracture. As the friction dissipation on the guideway was very low, the loss of kinetic energy was transformed into the strain energy of both the sample and the loading part. Typical high-speed videos of the dynamic out–in and in–out bending are shown in Movies 1 and 2, respectively.

After the bending test, all 36 fractured samples (24 from static bending and 12 from dynamic bending) were sputter-coated with gold–palladium (10 nm thickness) and observed using the Hitachi S-4800 SEM at an accelerating voltage of 3 kV to investigate the fracture patterns caused by the different loadings. The thickness and width at the fracture site of the samples in the dynamic test were also measured using a 3D macroscope (VR-3100, Keyence Corp., Osaka, Japan) to calculate the toughness of the samples under dynamic bending.

Estimation of mechanical resistance under out–in and in–out bending

Inverse FE optimization technology was used to calculate the mechanical properties of the shell sample based on the bending measurements. First, the three-dimensional geometrical models of all 36 beam shell samples were reconstructed based on the microCT image stacks using Amira 3D image analysis software (FEI Visualization Sciences Group, Bordeaux, France), meshed by eight-node hexahedral elements in Truegrid software (XYZ Scientific Application Inc., Livermore, CA, USA), and simulated using commercial LS-DYNA software (Livermore Software Technology Corp., Livermore, CA, USA). The boundary and loading conditions were the same as for the experimental settings. The fixture apparatus of the bending test was homogeneous isotropic linear elastic with an elastic modulus of 207 GPa and a Poisson's ratio of 0.3. The contacting behaviors between the samples and the fixture apparatus were defined as frictionless. A comparison of the deformation–load results between the current and a double-meshed FE model revealed a difference of less than 3%, indicating that the current element density was enough to satisfy mesh convergence.

The inverse FE optimizations for determining the mechanical resistance of the *M. edulis* shell under the different bending tests were implemented using LS-OPT software (Livermore Software Technology Corp.) (Fig. 3D). In the optimization, the objective function was the resultant force values of the loading part for the simulations of static bending but the strain energy of both the samples and loading part for the simulations of dynamic bending. The elastic modulus of the shell sample was calculated after a few iterations to minimize the difference between the simulated and experimental results of the objective function. The static and dynamic ultimate strengths were then acquired as the maximal absolute value between the maximal compressive and maximal tensile stress in the shell sample under static and dynamic bending, respectively. In addition, the toughness of the shell samples under

dynamic bending was calculated by dividing the total strain energy of the sample by the cross-sectional area of the samples at the fracture site.

Statistical analysis

One-way analysis of variance (ANOVA) was used to identify significant differences in the mass loss of the different shell layers due to the etching. The change of the contact area and angle caused by the etching was analyzed by repeated one-way ANOVA. A Bonferroni adjustment was chosen for all multiple comparisons. A two-tailed *t*-test was used to compare the mechanical properties of the shell (elastic modulus and ultimate strength from the static and dynamic bending and toughness from the dynamic bending) under the out–in and in–out bending tests. Significance for all the statistical tests was defined at the level $P<0.05$. Results are shown as means±s.d.

RESULTS

The etching results of the shell layers are shown in Fig. 4. The mass loss in groups A, B and C was 0.21±0.25, 0.25±0.20 and 0.76±0.39 mg, corresponding to the periostracum, prismatic and nacreous layers of the mussel shell, respectively. The nacreous layer was etched significantly more than the other two layers ($P<0.05$), such that its mass loss was approximately 3 times that of the others (Fig. 4A; Table S1). The wettability results indicate that the contact area of the droplet on the prismatic and nacreous layers was 3.2±0.32 and 2.9±0.20 mm² before acid etching and became 2.8±0.35 and 3.0±0.23 mm² after acid etching, respectively. There was no significant difference between the contact area on these two layers and the contact area was not altered by etching (Fig. 4B; Table S2). In contrast, a significant difference was found in the contact angle of the two shell layers before and after etching (Fig. 4C; Table S3). Before acid etching, the contact angle on the prismatic layer was significantly smaller than that on the nacreous layer ($P<0.05$). After acid etching, the contact angle on the prismatic layer increased significantly from 61±3.7 to 73±4.6 deg, whilst that on the nacreous layer did not change (68±3.5 versus 69±4.7 deg).

The SEM images of the different shell layers before and after the acid etching revealed the change of the microstructure under acid etching. When the periostracum of the shell was intact (i.e. group A), the etching from outside firstly destroyed the periostracum and subsequently corroded the exposed prismatic layer in the form of corrosive pitting (Fig. 4D). When the periostracum was removed (i.e. group B), the prismatic layer was etched directly to give an even corroded surface (Fig. 4G). Compared with the oblique prismatic crystals on the unetched region of the prismatic layer (Fig. 4E,H), a thin film (thickness of hundreds nanometers) was always observed above the prismatic crystals under both direct etching (i.e. no periostracum) and indirect etching (i.e. after corrosion of the periostracum; Fig. 4F,I). By contrast, no protective film was found on the etched nacreous surface (Fig. 4L). Comparison between the etched and unetched nacreous layer in group C illustrated that the dissolution of the nacre layer under acid etching originated from the organic matrix between the platelets, propagated into the intra-platelet, and resulted in separated nacreous platelets with a jagged surface at their sutural edges (Fig. 4K,L).

Fig. 5 shows the mechanical resistance results for the *M. edulis* shell against the out–in and in–out bend loadings. Under static out–in bending, the stiffness and strength of the *M. edulis* shell were 27.7±9.12 GPa and 131±27.0 MPa, significantly lower than those under static in–out bending, i.e. 39.8±9.54 GPa and 171±45.5 MPa. In contrast, under dynamic out–in bending, the stiffness and
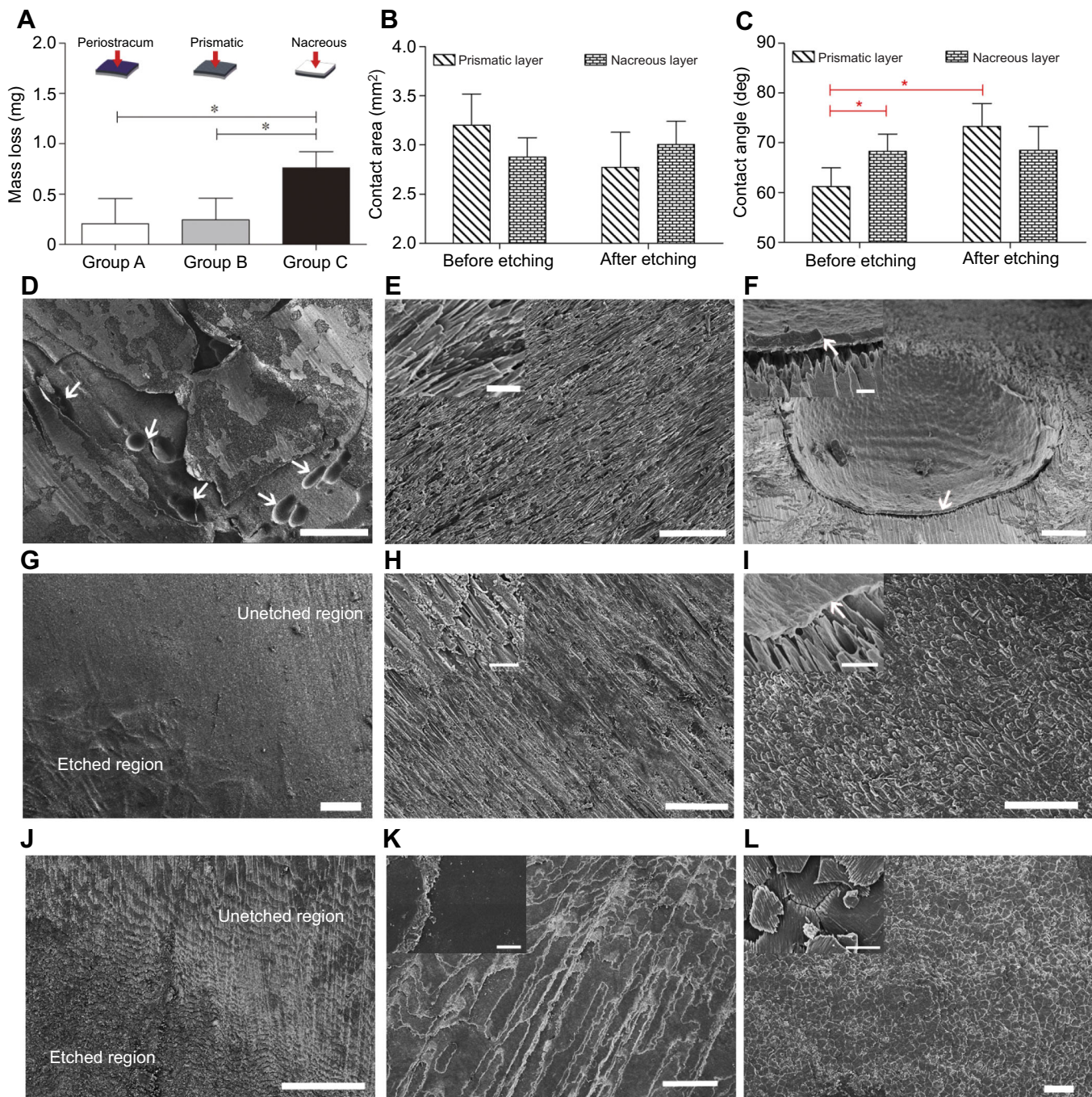
Fig. 4. The change in different shell layers under acid etching. (A) Mass loss caused by etching on the nacreous layer of the shell (group C, n=6) was significantly greater than that on the periostracum layer (group A, n=6) and the prismatic layer (group B, n=6). (B) There was no significant difference in the contact area of the water droplet on the etched versus unetched prismatic and nacreous surfaces of the shell, meaning that the variation of the mass loss was not the result of some potential change of contact area (group D, n=6). (C) Water contact angle on different shell surfaces. A significantly smaller contact angle was observed on the unetched prismatic layer compared with that on the unetched nacreous layer. A significantly greater contact angle was observed on the etched prismatic layer compared with that on the unetched prismatic layer (group D, n=6). Data in A–C are means±s.d. *P<0.05. (D) The etched surface in group A showed a destroyed periostracum and corrosive pitting on the exposed prismatic layer (marked by white arrows). (E,F) Unetched (E) and etched (F) surfaces of the prismatic layers. (G–I) The surface of group B after the etching test (G) with its unetched (H) and etched regions (I). A thin film generated on the prismatic layer is marked by white arrows in F and I. (J–L) The nacreous surface of group C after the etching test (J), and the unetched (K) and etched regions (L) on the nacreous surfaces. The microstructures of the unetched surface shown in E, H and K were caused by the polishing treatments, which were carried out to remove the periostracum or residual mantle tissues. Insets in the SEM images in the middle and right columns (E,F,H,I,K,L) are at high magnification to show surface topography details. Scale bars: D, 500 μm; G, 200 μm; J, 100 μm; E,F,H,I,K,L, 20 μm and 2 μm (insets).

strength of the *M. edulis* shell were 2.7±0.77 GPa and 11±2.9 MPa, not significantly different from those under dynamic in–out bending, i.e. 2.3±1.1 GPa and 10±3.8 MPa. The toughness of the *M. edulis* shell was 0.040±0.016 and 0.049±0.013 J mm^{-2} under dynamic out–in and in–out bending, respectively. The data for the static and dynamic mechanical tests are given in Tables S4 and S5.
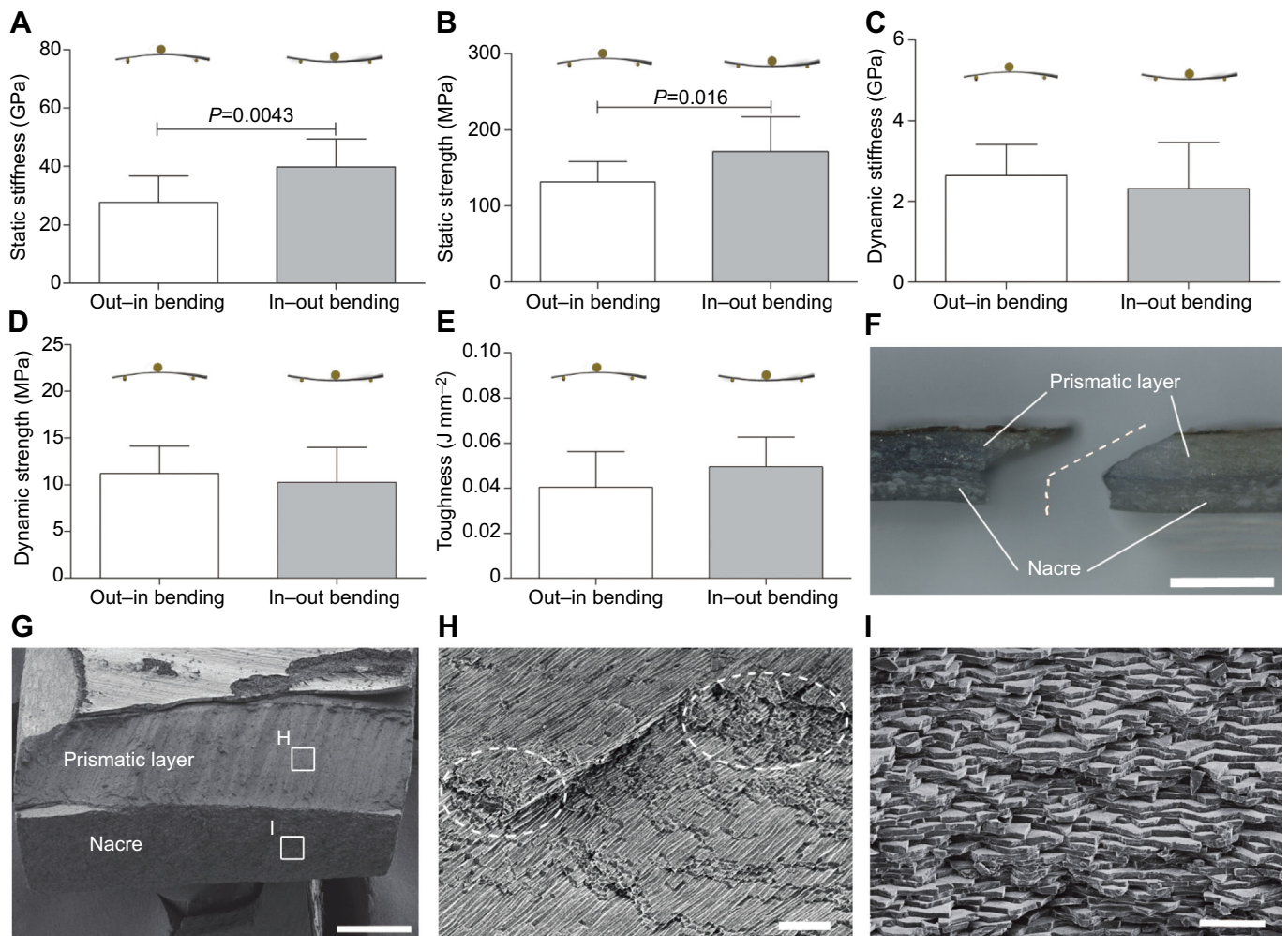
Fig. 5. Mechanical properties of shell beam samples under out–in and in–out bending tests. (A–E) Static stiffness (A) and strength (B), dynamic stiffness (C) and strength (D), and toughness (E) calculated from the out–in and in–out bending tests. n=12 for A and B; n=6 for C–E. The beam shell samples showed a similar fracture surface regardless of bending direction (out–in/in–out) and loading type (static/dynamic). Data in A–E are means±s.d. (F) Lateral view of the fractured beam sample (dog-leg fracture path is marked by the white dashed line). (G) SEM image of the fracture surface of the beam sample. (H,I) Detailed view of microstructures of the fracture surface on the prismatic layer (H) and nacre (I). In H, the fracture surface appeared as broken calcite grains (marked by a white dashed cycle) and cracks between the grains. In I, the fracture type at the micro-scale was tortuous, appearing as separation of intact individual platelets. Scale bars: F, 800 µm; G, 500 µm; H,I, 10 µm.

The fracture patterns of the shells were similar regardless of loading speed and direction. The global fracture surface of the prismatic layer was oblique and generally parallel to the longitudinal axis of the calcite grain (Fig. 5F,G). At the microstructure level, some cracks occurred in the organic matrix between the calcite grains while some appeared as fractures of the prismatic calcite (Fig. 5H). By contrast, the global fracture surface of the nacre was generally parallel to the loading direction but its micro-scale path was clearly of great tortuosity: cracks occurred between the aragonite platelets, resulting in separation of intact individual platelets (Fig. 5I).

DISCUSSION
The dissolution rate of the calcium carbonate-containing material depends on a few factors such as crystal size, the presence and distribution of organic matrix, etc. (Harper, 2000). Gabriel (1981) previously compared the resistance abilities of six biogenic calcitic shells against a simulated whelk attack and suggested that some non-nacreous structures are actually more effective in resisting predator boring, but the specific prismatic layer of the *M. edulis* shell was not included in the comparison. Therefore, to identify the

acid resistance of different layers in the *M. edulis* shell, the comparison should be performed on each specific layer. Harper (2000) measured the long-term dissolution rate of the prismatic layer of the *M. edulis* shell under sea water, but its acid resistance remained unclear. Our results indicated that the mass loss of the prismatic layer was approximately one-third that of the nacreous layer, implying that the prismatic layer of the *M. edulis* shell is stronger at resisting boring than the nacreous layer. Calcite is known to be 5–11% less soluble than aragonite under low acid concentrations (Weyl, 1959; de Visscher and Vanderdeelen, 2012), but this cannot account for the stronger acid resistance in the prismatic calcite layer. The similar contact area of the water droplet between these two layers (Fig. 4B) further illustrates that the differences in mass loss were not due to a possible change of the contact area. In contrast, the contact angle on the prismatic layer changed significantly after acid etching (Fig. 4C), meaning that some changes occurred on the etched surface. It was revealed from the SEM images that a thin film was generated above the prismatic crystals after acid etching. We suggest that this thin film accounts for the stronger resistance of the prismatic layer in the *M. edulis* shell

against acid attack. The main organic component of the shell is structural proteins, which are insoluble in water and acid (Keith et al., 1993; Sudo et al., 1997). Accordingly, the thin film is formed by the deposition of these acid-insoluble (AI) proteins gradually after the surrounding calcite grains have been dissolved. Unlike the AI proteins of the nacre whose function is suggested to induce biomineralization (Hou and Feng, 2006), the AI proteins of the prismatic layer seem to provide a protective shield for retarding dissolution of the shell by acidic fluids. From the perspective of chemical protection, it is advantageous that the prismatic layer appears as the outer layer of the *M. edulis* shell.

In this paper, we systematically investigated the protection performance of the bivalve mussel *M. edulis* shell against chemical and mechanical threats to identify potential reasons why nacre is deposited on the inside rather than on the outside of the shell. The results of bending tests depend on both the mechanical properties and the geometry of the samples. The sample geometry was reconstructed in FE models, including uneven thickness, curvature and dimensional scale. Therefore, the mechanical properties of the shell could be determined properly and accurately by inverse FE optimization, because the effect of sample geometry was taken into account in the FE models. We found that the mechanical resistance of the *M. edulis* shell appeared significantly stronger under static in–out bending than that under static out–in bending, in terms of both stiffness and strength. This implies that the shell would be endowed with a better defense against a slow (quasi-static) mechanical attack by predators if the nacre was in the outer layer. Specifically, the stiffness and strength of the *M. edulis* shell under static in–out bending increased by 30–40% compared with those under static out–in bending. This enhancement can be explained by the different stress conditions in the nacre. During the out–in and in–out bending tests, the nacre layer was loaded with tensile and compressive strains, resulting in tensile and compressive stress, respectively. The compressive modulus and strength (parallel to the shell layers) of sheet nacre samples from pearl oysters are 70 GPa and 370 MPa, while the tensile modulus and strength are <3 GPa and 140 MPa, respectively (Wang et al., 2001). Similar measurements were obtained for columnar nacre samples from red abalone, showing that the compressive strength is 38% higher than the tensile strength, i.e. 235 MPa versus 170 MPa (Menig et al., 2000; Meyers et al., 2008). The deformation mechanism of the nacre can account for this difference: in tension, the deformation originates mainly from wavy tablet sliding, whereas in compression, it originates from the aragonite tablet itself (Wang et al., 2001; Barthelat et al., 2007, 2016). Therefore, the *M. edulis* shell can manifest a stronger mechanical resistance under static in–out bending.

In contrast, the mechanical resistance of the *M. edulis* shell against dynamic out–in bending was similar to that against dynamic in–out bending. This signifies that the position of the nacre layer does not affect the protection ability of the *M. edulis* shell against dynamic mechanical attack. Compared with the static mechanical results, the stiffness and strength of the *M. edulis* shell under dynamic bending decreased by one order of magnitude. This finding is inconsistent with results previously obtained for *Haliotis rufescens* (abalone) and *Strombus gigas* (conch) shells, which showed that the dynamic compressive strength is approximately 50% higher than the quasi-static strength for both of these species (Menig et al., 2000, 2001). This discordance can be attributed to the difference in their shell structures. The abalone shell has a few nacreous mesolayers (each approximately 300 μm thick), which are separated by layers of viscoplastic material (each approximately 20 μm thick) (Menig et al., 2000). In addition, the aragonite tablets

in the mesolayers are deposited in the form of columns, differing from the sheet nacre of the *M. edulis* shell (Sun and Bhushan, 2012). The conch shell microstructure is also different from that of the *M. edulis* shell: the conch shell possesses a crossed-lamellar structure, three macrolayers, each composed of first-, second- and third-order lamellae (Menig et al., 2001).

The different structures of the shells reveal distinct fracture mechanisms, an important mechanical property of the shell. The fracture surface of the *M. edulis* shell revealed a few similar fracture features to those in the pearl oyster shell (Currey, 1977): the cracks in the nacre layer always occurred in the organic matrix between the aragonite platelets, in the form of separation of intact individual platelets; the fracture surface of the nacre layer was of great tortuosity (Fig. 5I), because the crack propagated in the weakest path within the material, demonstrating so-called crack deflection (Abid et al., 2019). Yet, plastic microbuckling (kinking) observed between the mesolayers of the abalone shells (Menig et al., 2000) was not found in the *M. edulis* shell under either static or dynamic bending tests. The plastic microbuckling can enhance the mechanical resistance of the abalone shell by dissipating the power from mechanical loadings, and is one of the most important damage-control mechanisms for the abalone shell (Menig et al., 2000). The lack of microbuckling might cause the dynamic mechanical resistance of the *M. edulis* shell to be greatly weaker than that of the abalone shell. High-speed camera recordings of the fracture region need to be performed in the future in order to provide details of crack initiation and development in the shell under different loading conditions.

In summary, our results indicate that the outer prismatic layer offers the *M. edulis* shell stronger resistance against the etching attack of predators, while better protection against slow mechanical attacks could be potentially achieved if nacre formed on the outside of the shell. The dynamic mechanical properties of the shell are the same independent of the outside or inside location of the nacre. The natural layering of materials in the *M. edulis* shell (outside, prismatic calcite, and inside, nacreous aragonite) has evolved as a compromise between sufficient resistance against etching attacks and protection against mechanical attacks. To endure the complex environment surrounding an organism, biological systems evolved as a result of optimization according to multiple objectives rather than single one (Ortiz and Boyce, 2008). The present study not only provides a deeper understanding of the biological material design of the mussel shell system but also may guide engineers to develop shell-inspired materials compromising different environmental factors for a variety of applications in robotics, defense systems or maritime technology. In the future, similar tests could be implemented on a large set of bivalve species to verify whether the compromise suggested by our results is a general feature for other bivalve mollusks.

Competing interests
The authors declare no competing or financial interests.

Author contributions
Conceptualization: C.W., S.N.G.; Methodology: C.W., Y.M., S.N.G.; Software: C.W., Y.M.; Formal analysis: C.W., Y.M.; Investigation: S.N.G.; Writing - original draft: C.W.; Writing - review & editing: C.W., Y.M., S.N.G.; Supervision: S.N.G.; Funding acquisition: C.W.

Supplementary information

Supplementary information available online at
http://jeb.biologists.org/lookup/doi/10.1242/jeb.201103.supplemental

References

Abid, N., Pro, J. W. and Barthelat, F. (2019). Fracture mechanics of nacre-like materials using discrete-element models: effects of microstructure, interfaces and randomness. *J. Mech. Phys. Solids* **124**, 350-365. doi:10.1016/j.jmps.2018.10.012

Arivalagan, J., Yarra, T., Marie, B., Sleight, V. A., Duvernois-Berthet, E., Clark, M. S., Marie, A. and Berland, S. (2016). Insights from the shell proteome: biomineralization to adaptation. *Mol. Biol. Evol.* **34**, 66-77. doi:10.1093/molbev/msw219

Barthelat, F. and Espinosa, H. D. (2007). An experimental investigation of deformation and fracture of nacre–mother of pearl. *Exp. Mech.* **47**, 311-324. doi:10.1007/s11340-007-9040-1

Barthelat, F., Tang, H., Zavattieri, P. D., Li, C. M. and Espinosa, H. D. (2007). On the mechanics of mother-of-pearl: a key feature in the material hierarchical structure. *J. Mech. Phys. Solids* **55**, 306-337. doi:10.1016/j.jmps.2006.07.007

Barthelat, F., Yin, Z. and Buehler, M. J. (2016). Structure and mechanics of interfaces in biological materials. *Nat. Rev. Mater.* **1**, 1-16. doi:10.1038/natrevmats.2016.7

Bonderer, L. J., Studart, A. R. and Gauckler, L. J. (2008). Bioinspired design and assembly of platelet reinforced polymer films. *Science* **319**, 1069-1073. doi:10.1126/science.1148726

Currey, J. D. (1977). Mechanical properties of mother of pearl in tension. *Proc. R. Soc. Lond. B.* **196**, 443-463. doi:10.1098/rspb.1977.0050

Day, J. F. (1969). Feeding of the cymatiid gastropod, *Argobuccinum argus*, in relation to the structure of the proboscis and secretions of the proboscis gland. *Am. Zool.* **9**, 909-916. doi:10.1093/icb/9.3.909

de Visscher, A. and Vanderdeelen, J. (2012). IUPAC-NIST solubility data series. 95. alkaline earth carbonates in aqueous systems. part 2. Ca. *J. Phys. Chem. Ref. Data* **41**, 023105. doi:10.1063/1.4704138

Fänge, R. and Lidman, U. (1976). Secretion of sulfuric acid in *Cassidaria echinophora* Lamarck (Mollusca: Mesogastropoda, marine carnivorous snail). *Comp. Biochem. Phys. A* **53**, 101-103. doi:10.1016/S0300-9629(76)80019-9

Gabriel, J. M. (1981). Differing resistance of various mollusc shell materials to simulated whelk attack. *J. Zool. Lond.* **194**, 363-369. doi:10.1111/j.1469-7998.1981.tb04587.x

Gao, H., Ji, B., Jager, I. L., Arzt, E. and Fratzl, P. (2003). Materials become insensitive to flaws at nanoscale: lessons from nature. *Proc. Natl. Acad. Sci. USA* **100**, 5597-5600. doi:10.1073/pnas.0631609100

Harper, E. M. (2000). Are calcitic layers an effective adaptation against shell dissolution in the Bivalvia? *J. Zool. Lond.* **251**, 179-186. doi:10.1111/j.1469-7998.2000.tb00602.x

Hou, W.-T. and Feng, Q.-L. (2006). Morphologies and growth model of biomimetic fabricated calcite crystals using amino acids and insoluble matrix membranes of *Mytilus edulis*. *Cryst. Growth Des.* **6**, 1086-1090. doi:10.1021/cg0504861

Jackson, A. P., Vincent, J. F. V. and Turner, R. M. (1988). The mechanical design of nacre. *Proc. R. Soc. Lond. B* **234**, 415-440. doi:10.1098/rspb.1988.0056

Keith, J., Stockwell, S., Ball, D., Remillard, K., Kaplan, D., Thannhauser, T. and Sherwood, R. (1993). Comparative analysis of macromolecules in mollusc shells. *Comp. Biochem. Physiol.* **105-B**, 487-496. doi:10.1016/0305-0491(93)90078-J

Mao, L.-B., Gao, H.-L., Yao, H.-B., Liu, L., Cölfen, H., Liu, G., Chen, S.-M., Li, S.-K., Yan, Y.-X., Liu, Y.-Y. et al. (2016). Synthetic nacre by predesigned matrix-directed mineralization. *Science* **354**, 107-110. doi:10.1126/science.aaf8991

Menig, R., Meyers, M. H., Meyers, M. A. and Vecchio, K. S. (2000). Quasi-static and dynamic mechanical properties of *Haliotis rufescens* (abalone) shells. *Acta. Mater.* **48**, 2383-2398. doi:10.1016/S1359-6454(99)00443-7

Menig, R., Meyers, M. H., Meyers, M. A. and Vecchio, K. S. (2001). Quasi-static and dynamic mechanical response of Strombus gigas (conch) shells. *Mater. Sci. Eng. A* **297**, 203-211. doi:10.1016/S0921-5093(00)01228-4

Meyers, M. A., Chen, P.-Y., Lin, A. Y.-M. and Seki, Y. (2008). Biological materials: structure and mechanical properties. *Prog. Mater. Sci.* **53**, 1-206. doi:10.1016/j.pmatsci.2007.05.002

Moody, K. E. and Steneck, R. S. (1993). Mechanisms of predation among large decapod crustaceans of the Gulf of Maine Coast: functional vs. phylogenetic patterns. *J. Exp. Mar. Biol. Ecol.* **168**, 111-124. doi:10.1016/0022-0981(93)90118-8

Morton, B. (2015). The feeding strategy of the predatory *Gyrineum natator* (Gastropoda: Neotaenioglossa: Ranellidae) in the Cape d'Aguilar Marine Reserve, Hong Kong, with a review of sulphuric acid use in prey access by the Tonnoidea and experimentally derived estimates of consumption. *J. Nat. Hist.* **49**, 483-507. doi:10.1080/00222933.2014.953614

Ortiz, C. and Boyce, M. C. (2008). Bioinspired structural materials. *Science* **319**, 1053-1054. doi:10.1126/science.1154295

Podsiadlo, P., Kaushik, A. K., Arruda, E. M., Waas, A. M., Shim, B. S., Xu, J., Nandivada, H., Pumplin, B. G., Lahann, J., Ramamoorthy, A. et al. (2007). Ultrastrong and stiff layered polymer nanocomposites. *Science* **318**, 80-83. doi:10.1126/science.1143176

Shao, Y., Zhao, H.-P., Feng, X.-Q. and Gao, H. (2012). Discontinuous crack-bridging model for fracture toughness analysis of nacre. *J. Mech. Phys. Solids* **60**, 1400-1419. doi:10.1016/j.jmps.2012.04.011

Song, F., Zhou, J., Xu, X., Xu, Y. and Bai, Y. (2008). Effect of a negative Poisson ratio in the tension of ceramics. *Phys. Rev. Lett.* **100**, 245502. doi:10.1103/PhysRevLett.100.245502

Sudo, S., Fujikawa, T., Nagakura, T., Ohkubo, T., Sakaguchi, K., Tanaka, M., Nakashima, K. and Takahashi, T. (1997). Structures of mollusc shell framework proteins. *Nature* **387**, 563. doi:10.1038/42391

Sun, J. and Bhushan, B. (2012). Hierarchical structure and mechanical properties of nacre: a review. *RSC Adv.* **2**, 7617-7632. doi:10.1039/c2ra20218b

Wang, R. Z., Suo, Z., Evans, A. G., Yao, N. and Aksay, I. A. (2001). Deformation mechanisms in nacre. *J. Mater. Res.* **16**, 2485-2493. doi:10.1557/JMR.2001.0340

Weyl, P. K. (1959). The change in solubility of calcium carbonate with temperature and carbon dioxide content. *Geochim. Cosmochim. Ac.* **17**, 214-225. doi:10.1016/0016-7037(59)90096-1

Zhang, C. and Zhang, R. (2006). Matrix proteins in the outer shells of molluscs. *Mar. Biotechnol.* **8**, 572-586. doi:10.1007/s10126-005-6029-6

Supplementary Materials

Table S1. Mass loss of the shell samples due to the etching. The mass values before and after the etching were averaged by three measurements. Mass loss is calculated by subtracting the mass before the etching from the mass after the etching.

Group No.	Etching site	Sample No.	Mass before etching, mg	Mass after etching, mg	Mass loss, mg
Group A	Periostracum	EA_S1	92.73	92.53	0.20
		EA_S2	100.5	99.9	0.60
		EA_S3	43.80	43.63	0.17
		EA_S4	76.37	76.47	-0.10
		EA_S5	71.17	71.16	0.01
		EA_S6	69.17	68.80	0.37
Group B	Prismatic layer	EB_S1	96.50	96.07	0.43
		EB_S2	83.33	82.87	0.46
		EB_S3	113.5	113.6	-0.10
		EB_S4	101.9	101.6	0.30
		EB_S5	122.0	121.8	0.20
		EB_S6	71.57	71.37	0.20
Group C	Nacre	EC_S1	92.03	91.40	0.63
		EC_S2	87.33	86.17	1.16
		EC_S3	53.60	53.20	0.40
		EC_S4	85.77	85.13	0.64
		EC_S5	61.73	60.40	1.33
		EC_S6	90.13	89.73	0.40

Table S2. Contact area of water droplet on the shell samples of group D before and after the etching. Contact area values before and after the etching were averaged for three measurements.

Sample No.	Contact area on prismatic surface, mm^2		Contact area on nacre surface, mm^2	
	before etching	after etching	before etching	after etching
ED_S1	2.858	2.780	2.897	2.729
ED_S2	3.777	2.869	2.801	3.273
ED_S3	3.139	2.401	3.262	3.027
ED_S4	3.206	2.809	2.765	3.262
ED_S5	2.971	3.368	2.806	2.760
ED_S6	3.250	2.418	2.734	2.985

Table S3. Contact angle of water droplet on the shell samples of group D before and after the etching. The values are averages of the angles from three measurements.

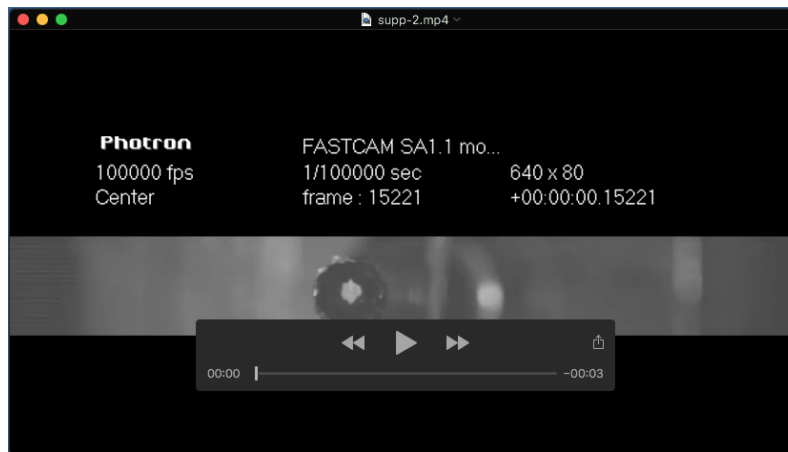| Sample No.	Contact angle on prismatic surface, °		Contact angle on nacre surface, °	
	before etching	after etching	before etching	after etching
ED_S1	61.3	75.5	71.3	73.5
ED_S2	60.1	73.5	69.0	60.8
ED_S3	65.3	76.6	71.2	72.3
ED_S4	61.0	67.8	70.3	65.8
ED_S5	54.9	67.7	63.8	70.9
ED_S6	64.7	78.6	64.1	67.9

Table S4. Static mechanical properties (elastic modulus and strength) of the beam shell samples under the out-in and in-out bending tests.

| Bending type	Sample No.	Static elastic modulus, GPa	Static ultimate strength, MPa
Out-in	SO_S1	14.7	129.7
	SO_S2	23.2	161.9
	SO_S3	30.3	86.1
	SO_S4	28.4	120.4
	SO_S5	26.1	140.2
	SO_S6	21.3	108.7
	SO_S7	41.2	181.8
	SO_S8	19.3	132.9
	SO_S9	27.3	125.5
	SO_S10	45.3	163.1
	SO_S11	35.0	105.9
	SO_S12	20.0	121.3
In-out	SI_S1	29.2	147.6
	SI_S2	41.3	154.2
	SI_S3	33.2	165.0
	SI_S4	35.3	170.7
	SI_S5	39.1	128.3
	SI_S6	53.9	228.6
	SI_S7	35.2	125.8
	SI_S8	54.4	184.6
	SI_S9	28.6	124.0
	SI_S10	34.3	175.1
	SI_S11	38.2	170.2
	SI_S12	55.0	282.0

Table S5. Dynamic elastic modulus, strength and toughness of the beam shell samples under the out-in and in-out bending tests.

Bending type	Sample No.	Dynamic elastic modulus, GPa	Dynamic ultimate strength, MPa	Toughness, J/mm²
Out-in	DO_S1	3.87	9.66	0.0157
	DO_S2	2.05	12.5	0.0439
	DO_S3	3.34	16.5	0.0609
	DO_S4	2.38	10.1	0.0418
	DO_S5	2.06	8.37	0.0291
	DO_S6	2.17	10.3	0.0504
In-out	DI_S1	1.67	8.02	0.0460
	DI_S2	1.23	6.50	0.0421
	DI_S3	2.23	9.95	0.0391
	DI_S4	3.24	11.6	0.0420
	DI_S5	1.44	8.25	0.0522
	DI_S6	4.13	17.1	0.0747

Movie 1. Typical high-speed video in recording the dynamic out-in bending of shell sample from its lateral view. The shell sample was shown in the middle of the field of view. The loading part of the impact tester translated from left to right in the video. Its velocity values before bending and after sample fracture were calculated by the movement of the white marker on its top surface.
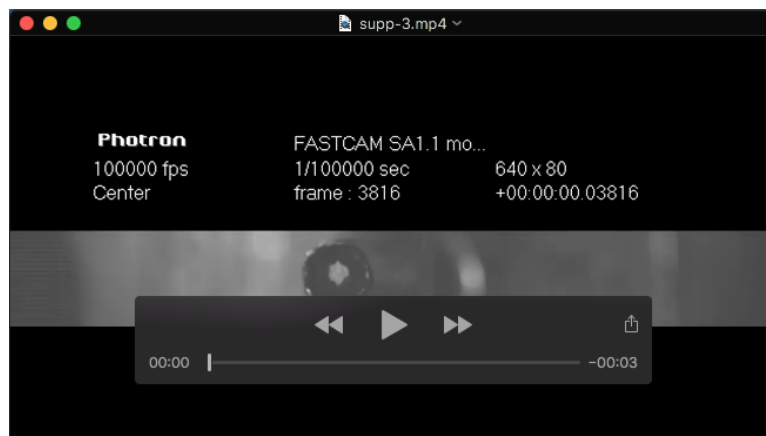
Movie 2. Typical high-speed video in recording the dynamic in-out bending of shell sample from its lateral view. The shell sample was shown in the middle of the field of view. The loading part of the impact tester translated from left to right in the video. Its velocity values before bending and after sample fracture were calculated by the movement of the white marker on its top surface.